Research Article | Vol. 30, No. 3 / 31 Jan 2022 / Optics Express 4434

Optics EXPRESS

# Uniformly scalable lithium niobate THz pulse source in transmission geometry

GERGŐ KRIZSÁN,[1,2,*] ZOLTÁN TIBAI,[1] GYÖRGY TÓTH,[1] PRIYO S. NUGRAHA,[2,3] GÁBOR ALMÁSI,[1] JÁNOS HEBLING,[1,2,3] AND JÓZSEF A. FÜLÖP[1,4]

[1]*Institute of Physics, University of Pécs, Pécs, Hungary*
[2]*Szentágothai Research Centre, University of Pécs, Pécs, Hungary*
[3]*MTA-PTE High-Field Terahertz Research Group, Pécs, Hungary*
[4]*ELI-ALPS, ELI-Hu Nonprofit Ltd., Szeged, Hungary*
[*]*krizsan@fizika.ttk.pte.hu*

**Abstract:** A novel THz source, based on optical rectification in $LiNbO_3$ using the tilted-pulse-front technique, is proposed and experimentally demonstrated. The pulse-front tilt is introduced by a volume phase holographic grating, efficiently used at perpendicular incidence in transmission, and the THz pulses are produced in a $LiNbO_3$ plane-parallel nonlinear echelon slab, arranged parallel to the grating. As a unique feature, the entire setup has a plane-parallel, transmission-type configuration, which straightforwardly enables distortion-free scaling to large sizes, high pulse energies and high THz field strengths. The possibility of operating the setup at cryogenic temperature for increased THz generation efficiency is also investigated. Calculations predict efficiencies of 95% for diffraction and 2% for THz generation at room temperature with a refractive-index-matching liquid between the grating and the echelon slab.



## 1. Introduction

Intense terahertz (THz) pulses can trigger nonlinear responses of materials by actively driving phonons, magnons, and other low-frequency modes to unprecedentedly large amplitudes. For example, the switching of magnetic order [1], novel insights into spin-lattice coupling [2], control and detection of spin order in antiferromagnets [3], introducing nonlinear effects on gases [4] and liquids [5,6], and acceleration of free electrons [7] were achieved. All these exciting applications depend on THz source technology delivering intense pulses. The highest so far peak field strengths have been achieved by optical rectification of ultrashort laser pulses in DSTMS (40 MV/cm [8]), GaSe (100 MV/cm [9]), and $LiNbO_3$ (LN, 6.3 MV/cm) [10] crystals. Among these, LN THz sources have found most widespread use due to the possibility of efficient pumping directly by Ti:sapphire and Yb lasers. This is in contrast to organic and semiconductor crystals, which require longer infrared pump wavelengths. Using conventional tilted-pulse-front technique, as high as 1.4 mJ pulse energy has been recently demonstrated from a cryogenically cooled LN source [10]. Despite such progress, up to now, the peak electric field strength produced in LN remained nearly one order of magnitude lower than that in the other two types of materials (DSTMS, GaSe), due to lower frequencies and other limitations.

The longest-standing problem with LN THz sources has been the strongly nonuniform interaction length across the beam in the prism-shaped nonlinear optical crystal. An early suggestion to solve this problem was to use a contact grating on the entrance surface of a LN plane-parallel slab [11]. However, the realization in LN turned out to be impossible [12], whereas the contact-grating concept was successfully demonstrated in a semiconductor nonlinear material [13–15]. Recently, new concepts have been proposed to reduce or solve the problem of nonuniform interaction length in LN tilted-pulse-front sources. In a conventional grating-lens-LN setup, it was proposed to replace the LN prism by a plane-parallel LN slab with an echelon

#440883 https://doi.org/10.1364/OE.440883
Journal © 2022 Received 18 Aug 2021; revised 13 Oct 2021; accepted 16 Nov 2021; published 28 Jan 2022

Optics EXPRESS

structure on its input surface [16]. In this case, a segmented tilted pulse front is produced, rather than a continuous one. THz generation was demonstrated from such an echelon-based source and the possibility of omitting the imaging was also mentioned [17]. An imaging-free LN wedge was also suggested, in which the wedged shape can compensate the spatially varying group delay dispersion. A wedge angle <10° can be used in this configuration, which is significantly smaller than the LN prism angle (~63°) in a conventional tilted-pulse-front setup [18]. Plane-parallel LN slabs with a reflection grating on the backside [19], or with an external reflection grating [20] were also investigated, which work in double higher (~±20) diffraction orders. These advances hold promise for a substantial increase of the achievable electric field strength to the multi-10-MV/cm level. However, to use a LN wedge, rather than a plane-parallel slab, still limits the lateral size of the source. Reflection-type approaches can be disadvantageous for some applications and the interference of the two overlapping diffracted beams can lead to reduced effective pump intensity [21].

In the present work, the nonlinear echelon slab (NLES) concept [16,17] is combined with an imaging-free approach in a way to maintain an ideal, laterally uniform pulse-front-tilting and THz-generation scheme in a transmission-type setup with a single diffraction order. This approach enables distortion-free, uniform scalability to large sizes, pump energies, and extreme focused THz field strengths. Specifically, the grating is used at perpendicular incidence, rather than in the conventional Littrow geometry. High diffraction efficiency (DE) can be achieved by using a volume phase holographic grating (VPHG) [22–24], rather than a binary one. This allows a completely plane-parallel grating-NLES configuration of transmission type, and is scalable without any principal limitation.

## 2. Setup

The proposed simple and compact THz pulse source setup is shown in Fig. 1. It is based on optical rectification in LN using the tilted-pulse-front technique [25]. The setup contains only two optical elements: a VPHG, which introduces the necessary pulse-front tilt (PFT), and the LN NLES, where the optical rectification takes place. The pump beam has normal incidence at the VPHG. Consequently, the diffraction angle and the PFT angle ($\gamma$) in the diffracted output beam will be equal and can be easily calculated in any material after the VPHG from the grating equation:

$$sin(\gamma) = \frac{\lambda_0}{nd}. \tag{1}$$

Here, $\lambda_0$ is the pump wavelength in vacuum, $d$ is the period of the grating and $n$ is the refractive index of the material between the VPHG and the NLES. The grating period $d$ is measured along the plane of the VPHG. More details on the VPHG are given in Section 3. In the diffracted output beam, the pulse front is parallel to the plane of the VPHG. This is essential for the parallelism, and hence, for the uniform scalability of the entire setup. This is in contrast to usual Littrow-type configurations, where the group delay dispersion, and consequently the pulse duration, is spatially varying across the beam.

The pump beam enters the NLES at normal incidence to the input facets of the echelon steps (Fig. 1), whereby its propagation direction and average PFT angle remain unchanged. Inside the LN nonlinear material, the pulse front becomes segmented [16], due to the discrete nature of the echelon steps. Thus, the local ($\gamma_{LN}$) and the average ($\gamma$) PFT angles will be different. Consequently, the pump pulse-front segmentation (more exactly, the $\gamma_{LN} < \gamma$ relation) results in dephasing between the elementary THz waves generated from different transversal positions inside the segments, causing a drop of the THz generation efficiency [16,18]. The local tilt angle of the individual pulse-front segments (Fig. 1) is determined by the following simple equation

Optics EXPRESS

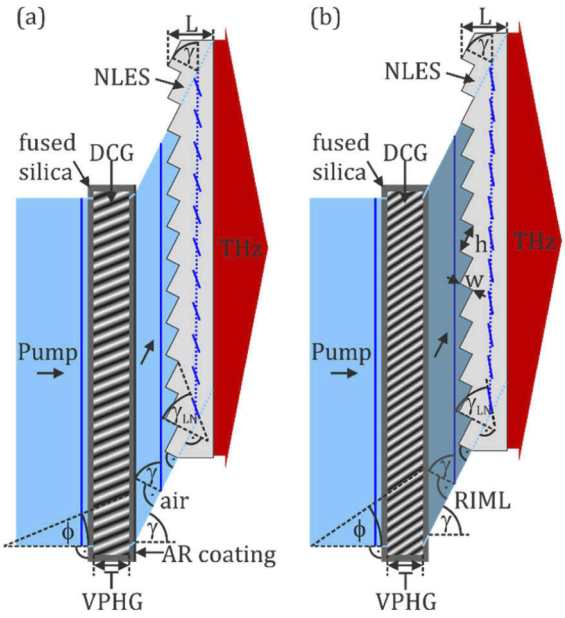


**Fig. 1.** NLES-VPHG THz sources. (a) Air-spaced configuration with antireflection (AR) coating at the VPHG backside. (b) RIML-filled configuration.

[26,27]:

$$\tan(\gamma_{\mathrm{LN}}) = \frac{n_{\mathrm{g}}}{n_{\mathrm{g,LN}}} \tan(\gamma). \tag{2}$$

Here, $n_{\mathrm{g}}$ is the group refractive index of the material filling the space between VPHG and NLES, and $n_{\mathrm{g,LN}}$ is the group refractive index of LN. For efficient THz generation in LN, an average PFT angle of $\gamma = 63°$ is needed at room temperature. Figure 1(a) shows the simplest, air-spaced configuration ($n_{\mathrm{g}} \approx 1$). It is useful to apply antireflection coating on the back side of the VPHG to reduce reflection losses at the grating window-air boundary (see also Section 3 for more details on the structure of the VPHG).

Obviously, according to Eq. (2), the mismatch between the average and the local PFT angles can be reduced by using refractive-index matching liquid (RIML) between the VPHG and the NLES. In such a RIML-filled configuration (Fig. 1(b)), the THz generation efficiency and the bandwidth can be increased by reducing the dephasing related to pulse-front segmentation. Furthermore, the RIML also reduces the Fresnel losses at the VPHG-liquid and liquid-LN boundaries.

The THz pulse, generated by optical rectification inside the NLES, propagates perpendicularly to the average PFT and leaves the NLES perpendicularly to its backside flat exit surface (Fig. 1). The duration of an initially Fourier-limited pump pulse will rapidly increase, and its intensity decrease behind the VPHG due to the angular dispersion and the associated group-velocity dispersion [26,27]. Hence, the pump pulse needs to be prechirped to compensate for this. In a conventional chirped-pulse laser amplifier, detuning the grating compressor can be used to restore the short pulse duration within the NLES.

Numerical simulations were carried out for both the air-spaced and the RIML-filled setups to optimize their parameters and to estimate and compare their performances in terms of pump throughput into the NLES and THz generation characteristics. The pump throughput, including especially the DE at the VPHG, was estimated by numerical simulations using the COMSOL software. The results are described in Section 3. THz generation results, calculated by a model introduced in Ref. [18], are presented in Section 4.

Optics EXPRESS

## 3. VPHG designs

Diffraction in a VPHG arises from the periodic modulation of the refractive index [22–24]. This index modulation can be produced in photosensitive materials, such as photopolymers or dichromated gelatin (DCG), by intensity-modulated illumination. DCG has a large index modulation capability up to about $\Delta n_{DCG} \lesssim 0.15$ [28]. For such large index modulation, high DE (which depends on the product of the thickness and $\Delta n_{DCG}$) can be achieved in a thin grating, which enables a broad spectral bandwidth. It can have high laser-induced damage threshold of about 2 J/cm$^2$ for 800-fs pulses of 1053 nm wavelength [29]. The DCG is usually sealed between two optical windows (e.g. fused silica or BK7) to support it and to protect it from humidity and dust [30].

VPHGs have high DE when the Bragg condition is fulfilled. In order to achieve the Bragg condition, the planes of constant refractive index can be tilted (slanted), as indicated in Fig. 1. It is very advantageous for many applications that a high DE can be achieved in this way even for a large difference between the angle of incidence and the angle of diffraction, i.e. far away from the Littrow configuration preferred by many other grating types. To determine the necessary slant angle $\phi$ (Fig. 1.) for high DE, it is essential to know the average refractive index of the DCG, $n_{DCG}$. This is ~1.54 for the unprocessed DCG [31], ~1.50 for $\Delta n_{DCG}$<0.1, and can be as low as 1.25 for a highly processed ($\Delta n_{DCG}$>0.1) DCG [23].

The efficiencies calculated by numerical simulations in COMSOL for the air-spaced and the RIML-filled configurations are shown in Figs. 2(a) and 2(b), respectively, as functions of the index-modulated layer thickness ($T$) and the slant angle ($\phi$). The calculated values are the pump diffraction efficiencies (pump DE), which include the VPHG DE and the Fresnel losses up to the NLES input surface. In both cases, a pump laser wavelength of 1030 nm was used and the DCG was assumed to be sealed between fused silica windows.

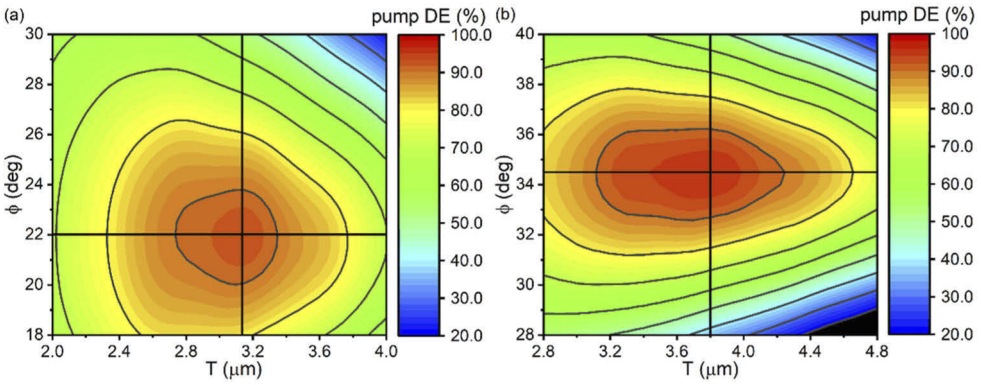


**Fig. 2.** Calculated pump DE up to the LN NLES as function of the index-modulated layer thickness ($T$) and the slant angle ($\phi$), in case of the air-spaced (a) and the RIML-filled (b) NLES-VPHG setups. The horizontal and vertical lines indicate the $T$ and $\phi$ values corresponding to the highest efficiencies.

For the air-spaced setup (Fig. 1(a)), a highly processed grating was supposed with $n_{DCG}$ = 1.35 and $\Delta n_{DCG}$ = 0.15. Antireflection (AR) coating was used only at the output side of the VPHG backside fused silica window. The maximum efficiency is 92.8%, if we suppose a multilayer AR coating with 2% loss. This efficiency can be achieved for $T$ = 3.15 μm index-modulated layer thickness and $\phi$ = 22.0° slant angle (Fig. 2(a)). (Without the AR coating at the backside, the efficiency is 77.4% for similar parameters, because of the higher Fresnel loss at the output surface.) Such efficiency is suitable to pump THz sources with a high conversion efficiency (see Section 4).

Optics EXPRESS

For the RIML-filled setup (Fig. 1(b)), a grating with $n_{DCG}$ = 1.5 and $\Delta n_{DCG}$ = 0.1 was supposed without AR coating at either side. A fused silica RIML was used with $n$ = 1.45 and with a group refractive index value of $n_g$ = 1.46. Because of the smaller Fresnel losses in the RIML-filled setup, a higher efficiency of 95.7% (Fig. 2(b)) can be achieved than in the air-spaced setup. Because of the smaller index modulation, the grating for the RIML-filled setup is thicker ($T$ = 3.8 μm) than in the air-spaced setup, which is required to achieve similarly high (>98%) internal diffraction efficiencies. In order to provide the same diffraction angle of $\gamma$ = 63°, the larger refractive index of the fused silica RIML requires a larger slant angle ($\phi$ = 34.5°) than in case of the air-spaced setup. We note that it is easier to manufacture a VPHG with parameters for the air-spaced setup, but the RIML-filled setup has more favorable output result. The parameters of the optimized air-spaced and RIML-filled setups are summarized in Table 1.

**Table 1. VPHG parameters of the two optimized designs.**

| Setup | Line density, $1/d$, (1/mm) | Average refractive index, $n_{\mathrm{DCG}}$ | Index modulation, $\Delta n_{\mathrm{DCG}}$ | Thickness of the index-modulated layer, $T$ (μm) | Slant angle, $\phi$ | DE (%) |
|---|---|---|---|---|---|---|
| Air-spaced | 865 | 1.35 | 0.15 | 3.15 | 22.0° | 92.8 |
| fused silica RIML-filled | 1297.5 | 1.5 | 0.1 | 3.8 | 34.5° | 95.7 |

It is of practical interest to investigate the possibility of cryogenic cooling the NLES-VPHG setups. Cooling can significantly enhance the THz generation efficiency by reducing the THz absorption in LN [32,33]. It was shown that the VPHG DE is not changing after several cooling and heating cycles [34]. Furthermore, it is possible to find a liquid with a suitably low freezing point and an appropriately high refractive index. One possible candidate is carbon disulfide with a refractive index of 1.595 [35] and freezing point of 162.35 K. (The fused silica RIML considered above enables cooling until about –40 °C and a moderate reduction of the THz absorption coefficient of LN [32,33]).

## 4. THz generation characteristics

Numerical simulations, based on the model described in Refs. [16,18], were performed to estimate the THz generation performance of the two NLES-VPHG setups and to compare them. The model takes into account the absorption of the LN nonlinear crystal in the THz range, the variation of the pump pulse duration along the propagation direction due to material and angular dispersions, the effect of dephasing with the increase of the transversal size of the segments along the propagation direction, and the Fresnel losses of the pump and the THz at the NLES front and output surfaces, respectively. Nonlinear interactions other than the generation of the THz field by optical rectification were not considered. Therefore, the calculations can be considered reliable up to about 2% pump-to-THz energy conversion efficiency [36]. In the simulations, pump pulses of 200 fs duration, 1030 nm central wavelength, and 70 GW/cm$^2$ peak intensity were assumed.

The THz generation efficiency as function of the NLES thickness ($L$) is shown in Fig. 3(a). The RIML-filled setup has up to about 1.8 times higher THz generation efficiency than the air-spaced one. Figure 3(b) gives the corresponding echelon step width $w$ (Fig. 1), optimized for each NLES thickness to give the highest THz generation efficiency. The height of the echelon steps (h) was calculated from the simple equation $\tan(\gamma) = h/w$ [16]. According to Fig. 3(b), the optimal echelon step width increases with increasing NLES thickness.

Three main factors determine the optimal stair step width. The diffraction and the dephasing effect of the tilted pulse front segments, and the material absorption at THz frequencies. With increasing step sizes, the pump pulse front segments will expand (because of the diffraction) less rapidly during propagation, the pump intensity can remain high for larger crystal thicknesses,

Optics EXPRESS

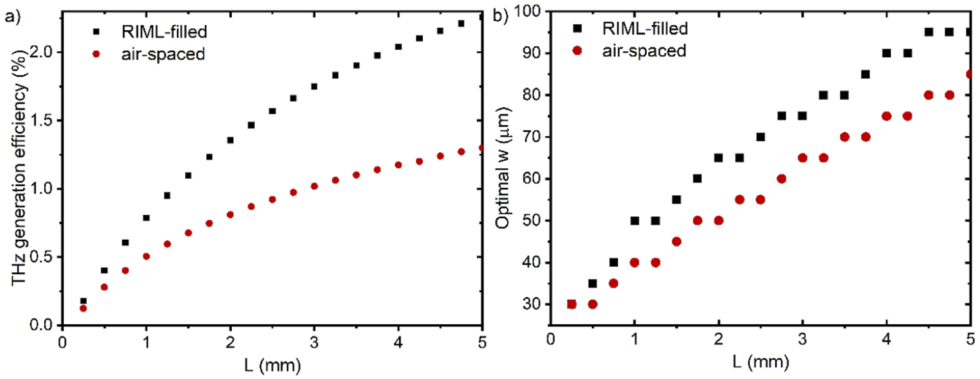


**Fig. 3.** (a) Pump-to-THz energy conversion efficiency and (b) optimal echelon step size (w) as functions of the NLES crystal thicknesses (L) of the air-spaced (red circles) and the RIML-filled (black squares) NLES-VPHG setups. The lines in part (b) are linear fits to the data points.

which can enable higher THz generation efficiency. On the other hand, with the increasing step size the dephasing effect will be stronger, which limits the THz generation efficiency, especially at higher frequencies. Furthermore, the material absorption also limits the THz frequencies that can be efficiently generated. The optimal step width shown in Fig. 3(b) represents a practical trade-off between these effects.

The calculated THz amplitude spectra and the temporal waveforms are plotted in Fig. 4 for both the air-spaced and the RIML-filled setups, in each case for 1.5 mm and 4 mm NLES thicknesses. In case of the air-spaced configuration, the peak of the amplitude spectrum is at 0.68 THz for 1.5 mm crystal thickness, and it is reduced to 0.43 THz for 4 mm. Similarly, in case of the RIML-filled configuration, the corresponding amplitude peaks are at 0.8 THz and 0.5 THz, respectively. The shift of the THz spectrum to lower frequencies with increasing crystal thickness is related to the increasing optimal echelon step width (Fig. 3(b)). By comparing the air-spaced to the RIML-filled setup, it is found that the bandwidth is broader, and the frequency of the amplitude peak is higher in the latter case. The reason for this is the smaller difference between the local and the average PFT angles, and the corresponding reduced dephasing effect,

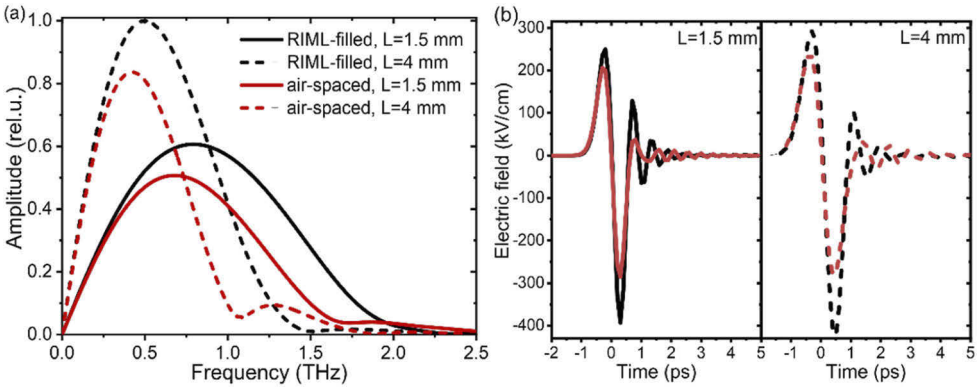


**Fig. 4.** Calculated amplitude spectra (a) and electric-field waveforms (b) of the air-spaced (red lines) and RIML-filled (black lines) setups, at 1.5 mm (solid lines) and 4 mm (dashed lines) NLES thicknesses.

Optics EXPRESS

as mentioned in Section 2. Figure 4(b) shows that nearly-single-cycle THz pulse shapes can be produced by both setups. The electric field values refer to the output side of the NLES in air, without any focusing.

## 5. Experimental results

A proof-of-principle experiment was carried out with the air-spaced setup (Fig. 1(a)). A VPHG (manufactured by Wasatch Photonics) with a grove density of 865 lines/mm was used, which had no AR coating at either side. The measured DE was 76% at normal incident and 63° angle of diffraction. This value is close to the simulated DE of 77.4%. The pump pulses had 1030 nm central wavelength, 200 fs transform-limited pulse duration, and up to 1 mJ energy. The NLES was the same prototype as in Ref. [17], with 5 mm height (parallel to the echelon grooves), 8 mm width, and $L = 3$ mm thickness. The width of the stair steps was $w = 50\ \mu m$. The prechirp of the pump pulses was set by adjusting the separation of the compressor gratings after the regenerative amplifier to maximize the THz output energy (see also Section 2). The THz pulse energy was measured after the LN NLES by a calibrated pyroelectric detector from Sensor- und Lasertechnik (THz 20) [37]. To get rid of any fundamental and second-harmonic beams, a PTFE (Teflon) window and a black paper were used between the NLES and the detector. Their THz transmissions were carefully calibrated and taken into account in the THz pulse energy measurements.

The experimental results for the air-spaced NLES-VPHG setup are shown in Fig. 5 (full symbols). The measured THz pulse energy was increasing nearly quadratically to about 0.2 μJ with increasing pump intensity to about 18 GW/cm$^2$. The pump-to-THz energy conversion efficiency was increasing up to about $3 \times 10^{-4}$. The reason for the relatively low efficiency can be attributed to the nonoptimal geometry of the prototype NLES and imperfections of the echelon surface, as discussed in more detail in Ref. [17]. The working of the NLES-VPHG principle with a high VPHG DE are demonstrated by comparing the THz yield of this new, imaging-free setup to the earlier demonstrated setup, which used a grating in Littrow configuration and imaging [17]. As it can be seen in Fig. 5, the THz generation efficiency in the two setups are nearly the

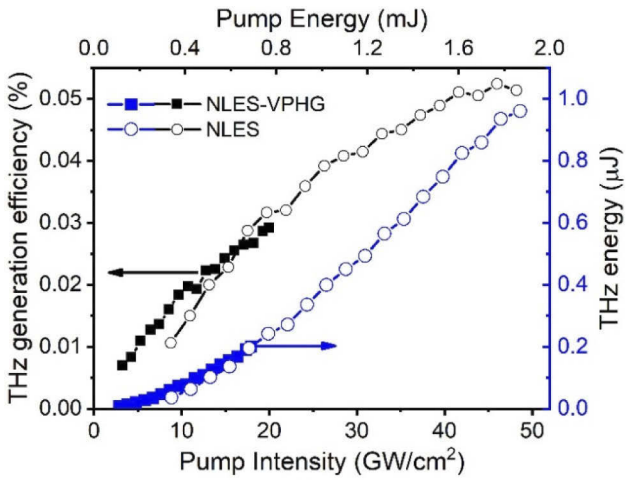


**Fig. 5.** Measured THz generation efficiency (full square symbols and left black axis) and THz pulse energy (full blue square symbols and right blue axis) as functions of the pump pulse intensity (bottom axis) and pump pulse energy (top axis) for the air-spaced NLES-VPHG setup. For comparison, the empty circles represent measured data for the NLES setup with a grating in Littrow configuration and imaging [17].

Optics EXPRESS

same. The empty symbols in Fig. 5 are for the earlier setup and show the same set of data as in Ref. [17]. We note that in both cases, the pump pulse energy was measured before the grating and its spot size was measured at the position of the NLES input surface. The predicted higher efficiencies and energies with the NLES-VPHG compared to the NLES with imaging will be accessible with larger VPHG-NLES sizes, where edge effects (imaging errors, and the longer pump pulse duration at the sides of the pump spot) can be significantly mitigated [16,17].

## 6. Conclusion

A novel THz source, based on optical rectification in $LiNbO_3$ using the tilted-pulse-front technique, is proposed and experimentally demonstrated. The pulse-front tilt is introduced by a volume phase holographic grating (VPHG). Such gratings can be used efficiently at perpendicular incidence in transmission, in contrast to the conventional Littrow configuration. THz pulses are produced in a $LiNbO_3$ plane-parallel nonlinear echelon slab (NLES). The compact, imaging-free setup has a plane-parallel, transmission-type geometry, which enables distortion-free scaling to large sizes, high pulse energies and THz field strengths. The setup can be operated at cryogenic temperatures for increased THz generation efficiency.

Two configurations were investigated: (i) a simple air-spaced one and (ii) one with refractive-index matching liquid (RIML) between the VPHG and the NLES (RIML-filled setup). Calculations predict similar VPHG diffraction efficiencies of 92.8% and 95.7%, for the two setups respectively. The RIML-filled setup is capable to deliver 1.8 times higher THz generation efficiency than the air-spaced one. Up to about 2% THz generation efficiency can be expected.

In a proof-of-principle experiment, similar THz generation efficiency was demonstrated with the air-spaced NLES-VPHG setup as achieved in our previous work in the same prototype NLES, but using a grating in conventional Littrow configuration and imaging optics for tilting the pump pulse front. This suggest that the NLES-VPHG setup can produce the same THz generation efficiency as the NLES with imaging, without any principal limitations in the useful pump beam diameter. The concept is adaptable to other materials, such as semiconductors. Because of the compact, straight-through transmission geometry, the NLES-VPHG concept can be easily adapted to various applications, pulse energies, and focusing conditions.

**Funding.** National Research, Development and Innovation Office (2018-1.2.1-NKP-2018-00009, 2018-1.2.1-NKP-2018-00010, 2018-2.1.5-NEMZ-2018-00003, Eurostars (E 12576 HABRIA), FK-OTKA-129134, NN-OTKA-125808, TKP2020-IKA-08).

**Acknowledgements.** Krizsán Gergő acknowledges support from the ÚNKP-20-3 New National Excellence Program of the Ministry for Innovation and Technology from the source of the National Research, Development and Innovation Office. György Tóth and Zoltán Tibai would like to thank the support of the János Bolyai Research Scholarship of the Hungarian Academy of Science.

**Disclosures.** The authors declare no conflicts of interest.

**Data availability.** The data that support the findings of this study are available within the article and from the corresponding author upon reasonable request.

## References

1. S. Schlauderer, C. Lange, S. Baierl, T. Ebnet, C. P. Schmid, D. C. Valovcin, A. K. Zvezdin, A. V. Kimel, R. V. Mikhaylovskiy, and R. Huber, "Temporal and spectral fingerprints of ultrafast all-coherent spin switching," Nature **569**(7756), 383–387 (2019).
2. S. F. Maehrlein, I. Radu, P. Maldonado, A. Paarmann, M. Gensch, A. M. Kalashnikova, R. V. Pisarev, M. Wolf, P. M. Oppeneer, J. Barker, and T. Kampfrath, "Dissecting spin-phonon equilibration in ferrimagnetic insulators by ultrafast lattice excitation," Sci. Adv. **4**(7), eaar5164 (2018).
3. P. Němec, M. Fiebig, T. Kampfrath, and A. V. Kimel, "Antiferromagnetic opto-spintronics," Nat. Phys. **14**(3), 229–241 (2018).
4. J. Lu, Y. Zhang, H. Y. Hwang, B. K. Ofori-Okai, S. Fleischer, and K. A. Nelson, "Nonlinear two-dimensional terahertz photon echo and rotational spectroscopy in the gas phase," Proc. Natl. Acad. Sci. **113**(42), 11800–11805 (2016).
5. V. Balos, G. Bierhance, M. Wolf, and M. Sajadi, "Terahertz-magnetic-field induced ultrafast Faraday rotation of molecular liquids," Phys. Rev. Lett. **124**(9), 093201 (2020).

Optics EXPRESS


6. H. Elgabarty, T. Kampfrath, D. J. Bonthuis, V. Balos, N. K. Kaliannan, P. Loche, R. R. Netz, M. Wolf, T. D. Kühne, and M. Sajadi, "Energy transfer within the hydrogen bonding network of water following resonant terahertz excitation," Sci. Adv. **6**(17), eaay7074 (2020).
7. D. Zhang, A. Fallahi, M. Hemmer, X. Wu, M. Fakhari, Y. Hua, H. Cankaya, A.-L. Calendron, L. E. Zapata, N. Matlis, and F. X. Kärtner, "Segmented terahertz electron accelerator and manipulator (STEAM)," Nat. Photonics **12**(6), 336–342 (2018).
8. C. Vicario, A. V. Ovchinnikov, S. I. Ashitkov, M. B. Agranat, V. E. Fortov, and C. P. Hauri, "Generation of 0.9-mJ THz pulses in DSTMS pumped by a Cr:Mg2SiO4 laser," Opt. Lett. **39**(23), 6632–6635 (2014).
9. A. Sell, A. Leitenstorfer, and R. Huber, "Phase-locked generation and field-resolved detection of widely tunable terahertz pulses with amplitudes exceeding 100 MV/cm," Opt. Lett. **33**(23), 2767–2769 (2008).
10. B. Zhang, Z. Ma, J. Ma, X. Wu, C. Ouyang, D. Kong, T. Hong, X. Wang, P. Yang, L. Chen, Y. Li, and J. Zhang, "1.4-mJ High Energy Terahertz Radiation from Lithium Niobates," Laser Photonics Rev. **15**(3), 2000295 (2021).
11. L. Pálfalvi, J. A. Fülöp, G. Almási, and J. Hebling, "Novel setups for extremely high power single-cycle terahertz pulse generation by optical rectification," Appl. Phys. Lett. **92**(17), 171107 (2008).
12. Z. Ollmann, J. Hebling, and G. Almási, "Design of a contact grating setup for mJ-energy THz pulse generation by optical rectification," Appl. Phys. B **108**(4), 821–826 (2012).
13. J. A. Fülöp, G. Polónyi, B. Monoszlai, G. Andriukaitis, T. Balciunas, A. Pugzlys, G. Arthur, A. Baltuska, and J. Hebling, "Highly efficient scalable monolithic semiconductor terahertz pulse source," Optica **3**(10), 1075–1078 (2016).
14. M. I. Bakunov and S. B. Bodrov, "Terahertz generation with tilted-front laser pulses in a contact-grating scheme," J. Opt. Soc. Am. B **31**(11), 2549–2557 (2014).
15. Z. Ollmann, J. A. Fülöp, J. Hebling, and G. Almási, "Design of a high-energy terahertz pulse source based on ZnTe contact grating," Opt. Commun. **315**, 159–163 (2014).
16. L. Pálfalvi, G. Tóth, L. Tokodi, Z. Márton, J. A. Fülöp, G. Almási, and J. Hebling, "Numerical investigation of a scalable setup for efficient terahertz generation using a segmented tilted-pulse-front excitation," Opt. Express **25**(24), 29560–29573 (2017).
17. P. S. Nugraha, G. Krizsán, C. Lombosi, L. Pálfalvi, G. Tóth, G. Almási, J. A. Fülöp, and J. Hebling, "Demonstration of a tilted-pulse-front pumped plane-parallel slab terahertz source," Opt. Lett. **44**(4), 1023–1026 (2019).
18. G. Tóth, L. Pálfalvi, J. A. Fülöp, G. Krizsán, N. H. Matlis, G. Almási, and J. Hebling, "Numerical investigation of imaging-free terahertz generation setup using segmented tilted-pulse-front excitation," Opt. Express **27**(5), 7762–7775 (2019).
19. G. Tóth, L. Pálfalvi, Z. Tibai, L. Tokodi, J. A. Fülöp, Z. Márton, G. Almási, and J. Hebling, "Single-cycle scalable terahertz pulse source in reflection geometry," Opt. Express **27**(21), 30681–30691 (2019).
20. G. Krizsán, Z. Tibai, J. Hebling, L. Pálfalvi, G. Almási, and G. Tóth, "Lithium niobate and lithium tantalate based scalable terahertz pulse sources in reflection geometry," Opt. Express **28**(23), 34320–34327 (2020).
21. G. Polónyi, M. I. Mechler, J. Hebling, and J. A. Fülöp, "Prospects of semiconductor terahertz pulse sources," IEEE J. Sel. Top. Quantum Electron. **23**(4), 1–8 (2017).
22. T. A. Shankoff, "Phase Holograms in Dichromated Gelatin," Appl. Opt. **7**(10), 2101–2105 (1968).
23. I. K. Baldry, J. Bland-Hawthorn, and J. G. Robertson, "Volume Phase Holographic Gratings: Polarization Properties and Diffraction Efficiency," Publ. Astron. Soc. Pac **116**(819), 403–414 (2004).
24. B. Pierre-Alexandre, G. Patrick, L. M. H. Serge, C. L. Philippe, and A. J. J. Claude, "Volume phase holographic gratings: large size and high diffraction efficiency," Opt. Eng. **43**(11), 2603–2612 (2004).
25. J. Hebling, G. Almási, I. Z. Kozma, and J. Kuhl, "Velocity matching by pulse front tilting for large-area THz-pulse generation," Opt. Express **10**(21), 1161–1166 (2002).
26. J. Hebling, "Derivation of the pulse front tilt caused by angular dispersion," Opt. Quantum Electron **28**(12), 1759–1763 (1996).
27. J. A. Fülöp and J. Hebling, "Applications of tilted-pulse-front excitation," in *Recent optical and photonic technologies*, K. Y. Kim, ed. (InTech, 2010).
28. L. D. Dickson, R. D. Rallison, and B. H. Yung, "Holographic polarization-separation elements," Appl. Opt. **33**(23), 5378–5385 (1994).
29. P. Rambo, J. Schwarz, and I. Smith, "Development of a mirror backed volume phase grating with potential for large aperture and high damage threshold," Opt. Commun. **260**(2), 403–414 (2006).
30. Samuel C. Barden, James A. Arns, Willis S. Colburn, and Joel B. Williams, "Volume-Phase Holographic Gratings and the Efficiency of Three Simple Volume-Phase Holographic Gratings," Publ. Astron. Soc. Pac **112**(772), 809–820 (2000).
31. D. R. Richard and R. S. Scott, "Polarization properties of gelatin holograms," Proc.SPIE **1667**, 266–275 (1992).
32. M. Unferdorben, Z. Szaller, I. Hajdara, J. Hebling, and L. Pálfalvi, "Measurement of refractive index and absorption coefficient of congruent and stoichiometric lithium niobate in the terahertz range," J. Infrared Millim. Terahertz Waves **36**(12), 1203–1209 (2015).
33. X. Wu, C. Zhou, W. R. Huang, F. Ahr, and F. X. Kärtner, "Temperature dependent refractive index and absorption coefficient of congruent lithium niobate crystals in the terahertz range," Opt. Express **23**(23), 29729–29737 (2015).

Optics EXPRESS

34. N. Tamura, G. J. Murray, P. Luke, C. Blackburn, D. J. Robertson, N. A. Dipper, R. M. Sharples, and J. R. Allington-Smith, "Cryogenic tests of volume-phase holographic gratings: results at 100 K," Appl. Opt. **45**(23), 5923–5928 (2006).
35. S. Kedenburg, M. Vieweg, T. Gissibl, and H. Giessen, "Linear refractive index and absorption measurements of nonlinear optical liquids in the visible and near-infrared spectral region," Opt. Mater. Express **2**(11), 1588–1611 (2012).
36. K. Ravi, W. R. Huang, S. Carbajo, X. Wu, and F. Kärtner, "Limitations to THz generation by optical rectification using tilted pulse fronts," Opt. Express **22**(17), 20239–20251 (2014).
37. Sensor- und Lasertechnik, "THz-Detectors" (06/07/2021, 2017), retrieved https://www.pyrosensor.de/THz-2017-pdf-922903.pdf.